SARS-CoV-2 causes brain inflammation and induces Lewy body formation in macaques

Ingrid H.C.H.M. Philippens[1,*†], Kinga P. Böszörményi[1†], Jacqueline A. Wubben[1], Zahra C. Fagrouch[1], Nikki van Driel[1], Amber Q. Mayenburg[1], Diana Lozovagia[1], Eva Roos[2], Bernadette Schurink[2], Marianna Bugiani[2], Ronald E. Bontrop[1,3], Jinte Middeldorp[1], Willy M. Bogers[1], Lioe-Fee de Geus-Oei[5,6], Jan A.M. Langermans[1,4], Marieke A. Stammes[1‡], Babs E. Verstrepen[1‡], Ernst J. Verschoor[1‡]

[1] Biomedical Primate Research Centre (BPRC), Lange Kleiweg 161, 2288GJ Rijswijk, The Netherlands

[2] Department of Pathology, Amsterdam UMC, De Boelelaan 1117, 1081HV Amsterdam, The Netherlands

[3] Department of Biology, Theoretical Biology and Bioinformatics, Utrecht University, Padualaan 8, Utrecht, The Netherlands

[4] Department Population Health Sciences, Division of Animals in Science and Society, Faculty of Veterinary Medicine, Utrecht University, Yalelaan 1, 3584CL Utrecht, The Netherlands

[5] Department of Radiology, Leiden University Medical Center, Albinusdreef 2, 2333ZA Leiden, The Netherlands

[6] Biomedical Photonic Imaging Group, University of Twente, Drienerlolaan 5, 7522ND Enschede, The Netherlands

† These authors contributed equally

‡ These authors jointly supervised this work

* Corresponding author. E-mail: philippens@bprc.nl

Keywords: SARS-CoV-2; macaques; brain inflammation; Lewy body formation; neuropathology; PET-CT

Abstract:

SARS-CoV-2 may cause acute respiratory disease, but the infection can also initiate neurological symptoms. Here we show that SARS-CoV-2 infection causes brain inflammation in the macaque model. An increased metabolic activity in the pituitary gland of two macaques was observed by longitudinal positron emission tomography-computed tomography (PET-CT). Post-mortem analysis demonstrated infiltration of T-cells and activated microglia in the brain, and viral RNA was detected in brain tissues from one animal. We observed Lewy bodies in brains of all rhesus macaques. These data emphasize the virus' capability to induce neuropathology in this nonhuman primate model for SARS-CoV-2 infection. As in humans, Lewy body formation is an indication for the development of Parkinson's disease, this data represents a warning for potential long-term neurological effects after SARS-CoV-2 infection.

Teaser:

SARS-CoV-2 causes brain inflammation and Lewy bodies, a hallmark for Parkinson, after an asymptomatic infection in macaques.

50 **Introduction**

51 Severe acute respiratory syndrome coronavirus 2 (SARS-CoV-2) causes a multi-system
52 inflammatory disease syndrome, COVID-19 (*1*). Although SARS-CoV-2 predominantly affects the
53 respiratory organs, over 30% of the hospitalized COVID-19 patients also suffer from neurological
54 manifestations, including loss of smell or taste, delirium, diminished consciousness, epilepsy, and
55 psychosis (*2-5*). Besides these general neurological symptoms, some patients additionally endure
56 Parkinsonism (*6-8*). The mechanisms behind this process are poorly understood. Neurological
57 symptoms may be triggered by infection of the brain tissue, or indirectly, via virus-induced
58 immune cell activation (*9*). In humans, a direct link between brain inflammation and the presence
59 of SARS-CoV-2 RNA has not been established yet (*10*), and thus, formal proof that central nervous
60 system (CNS)-related symptoms of COVID-19 are directly caused by the infection, or indirectly
61 due to overactivation of the immune system, is lacking. Additionally, the long-term effects on the
62 CNS after a mild to moderate SARS-CoV-2 infection, likely the vast majority of human cases, are
63 unknown, and post-mortem brain samples from these individuals are not expected to become
64 available for research in the near future. Controlled infection studies in a standardized
65 experimental setting are crucial to investigate SARS-CoV-2-induced brain pathology (*11*). To
66 address this issue, a study was performed in two macaques species, rhesus macaques (*Macaca*
67 *mulatta*) and cynomolgus macaques (*Macaca fascicularis)* (Table 1), both well-accepted animal
68 models for COVID-19 (*12*). Four male rhesus and four male cynomolgus macaques were
69 inoculated with 10^5 $TCID_{50}$ of SARS-CoV-2 strain BetaCoV/BavPat1/2020 via a combined
70 intratracheal and intranasal route (*13, 14*). Following infection, SARS-CoV-2 genomic material was

71 detected in tracheal and nasal swabs up to ten days, and based on clinical signs and thorax CTs,
72 all animals showed mild to moderate disease symptoms (*13, 15*).
73
74 **Results and Discussion**
75 Weekly ^{18}F-FDG PET-CTs of the brains of all macaques were initiated at the time point that the
76 virus became undetectable in nasal and tracheal swabs. The uptake of tracer renders a marker
77 for metabolic activity. Two of four cynomolgus macaques (C1 and C2) displayed an increased
78 uptake of ^{18}F-FDG in the pituitary gland at multiple time points. In animal C1, an increased uptake
79 of ^{18}F-FDG in the pituitary gland was seen at days 30 and 36 post-infection (Fig. 1). In animal C2,
80 increased metabolic activity was already visible on day 8 and continued through day 35 when the
81 final scan was obtained (Table S1).
82 In humans and macaques, the volume of the pituitary gland is small, and under physiological
83 conditions, its metabolic activity is comparable to the background level of the entire brain (*16,*
84 *17*). The ^{18}F-FDG uptake of the pituitary gland may even be underestimated due to the partial-
85 volume-effects that affect the emission signal recovery (*16*). Because pituitary gland tissue
86 expresses angiotensin-converting enzyme 2 (ACE2) (*18*), the increased ^{18}F-FDG uptake may be a
87 direct effect of the infection or an indirect effect due to either a (reversible) hypophysitis, or
88 transient hypothalamic-pituitary dysfunction (*19*). Hypocortisolism has been reported as a
89 delayed complication of SARS and has also been described in a SARS-CoV-2 patient (*20*). For
90 animal C1, which showed increased ^{18}F-FDG uptake 30 days after infection, it is likely that the
91 hypothalamic-pituitary axis was activated, leading to hypocortisolism similar to what has been
92 found in patients with both a SARS and SARS-CoV-2 infection.

93 To further investigate the consequences of SARS-CoV-2-infection on macaque brain tissue, the
94 animals were euthanized 5-6 weeks after experimental infection. Sections of the whole brain
95 were systematically collected for further examination. As several regions of the brain express the
96 SARS-CoV-2 receptor ACE2, and inflammation was found in the human brain (*10, 21, 22*), we used
97 various immunological markers for innate and adaptive immune activation to investigate for signs
98 of immune activation, and also explored the localization of virus particles (Fig. 2 and Table 2).
99 Viral RNA was detected by real-time quantitative polymerase chain reaction (RT-qPCR) in multiple
100 brain areas of the right hemisphere of cynomolgus macaque C3 (Fig. 2). More precisely,
101 cerebellum ($1.48x10^5$ RNA genome equivalents (GE)/gram), medial motor cortex ($2.09x10^5$
102 GE/gram), sensory cortex ($2.07x10^5$ GE/gram) and frontal basal cortex ($8.29x10^4$ GE/gram), as well
103 as hippocampus ($1.24x10^5$ GE/gram), hypothalamus ($1.05x10^6$ GE/gram), and globus pallidus
104 ($5.45x10^4$ GE/gram) all tested positive in the RT-qPCR. No viral RNA was detected in samples
105 collected from the pituitary gland or olfactory bulb, substantia nigra, medulla oblongata, pons,
106 nucleus caudatus, and putamen. Of interest, other tissues collected from macaque C3, including
107 tracheobronchial lymph nodes, heart, liver, spleen, and kidney, also tested positive in the RT-
108 qPCR, with comparable (lymph nodes, heart), or lower (kidney, liver, spleen) viral RNA loads (*13*).
109 Subgenomic messenger RNA analysis did not show evidence for active virus replication in the
110 brains at the time point of euthanasia. Additionally, SARS-CoV-2 antigen was not detectable by
111 immunohistochemistry the brains of all macaques.
112 The brains of all SARS-CoV-2-infected macaques showed evidence of inflammation. Presence of
113 T-cells was visualized by CD3 staining in intraparenchymal brain tissue, suggesting the infiltration
114 of T-cells that passed the blood-brain barrier after SARS-CoV-2 infection (Fig. 3A, top panel).

115 Additionally, activation of microglia cells in different areas of the brain, including the olfactory
116 bulb and pituitary gland, was confirmed by Mamu-DR staining (upregulation of MHC class II
117 expression) (Fig. 3A, middle panel). However, nodule formation, which is a measure for severity
118 of activation, was rarely present (Table 2). No B-lymphocytic infiltration was found as evidenced
119 by lack of CD20 staining (not shown). Hematoxylin and eosin (HE) staining did not show any
120 abnormalities in the brain tissue of the virus-exposed macaques, including the absence of
121 ischemic/necrotic lesions. For comparison, post-mortem brain tissues from two healthy, age-
122 matched macaques of each species were used as controls (Table 1), none of the four control
123 animals displayed obvious signs of immune activation (T-cells and microglia).
124 Brain tissues were screened for α-synuclein deposits, known as Lewy bodies, by
125 immunohistochemistry. In humans, Lewy body formation is linked to the development of
126 Parkinson's disease or Lewy body dementia (*23, 24*). It has been hypothesized that certain
127 neurotropic viruses, including MERS and SARS coronaviruses, can trigger formation of Lewy
128 bodies and cause Parkinsonism (*25-30*).
129 The formation of intracellular Lewy bodies was clearly shown in the ventral midbrain region next
130 to the caudate nucleus of all infected rhesus macaques (Table 2, Fig. 3B), and in one aged
131 cynomolgus macaque (C4), while Lewy bodies were absent in the brains of all four control
132 animals. For cynomolgus macaque C4, an age-dependent factor related to Parkinsonism cannot
133 be excluded as this animal was older (16 years) than the other panel members (5-7 years), but
134 the data from the rhesus macaques provide clear evidence for SARS-CoV-2-driven inflammation
135 in the brain of macaques. In humans, neuropathology has been described in moribund COVID-19
136 patients, but we report of SARS-CoV-2-related brain involvement in macaques without displaying

137 overt clinical signs. In general, macaque models for SARS-CoV-2 infection typically represent mild
138 to moderate COVID-19 symptoms on the CT scan compared to humans (*12, 14, 31*). Detection of
139 viral RNA in the brain of an animal demonstrates the virus' neuroinvasive capability. This matches
140 a recent study describing neuroinvasion in mouse brains and in human brain organoids (*32*).
141 How exactly SARS-CoV-2 caused widespread brain inflammation and induced Lewy body
142 formation remains unknown. Viruses can enter the brain via different pathways. In this study,
143 infiltration of T-cells was found perivascular and in the brain parenchyma, which indicates that
144 the blood-brain barrier integrity may have been disturbed, offering the virus the opportunity to
145 enter the brain. Alternatively, we hypothesize that SARS-CoV-2 gained access to the brain via
146 neuronal pathways, such as the retrograde and anterograde neuronal transport through infected
147 motor or sensory neurons (*33*), and entered the pituitary gland via binding to the ACE2 receptor
148 protein expressed on its cell surfaces (*18, 34*). Such neural connection also exists between the
149 olfactory bulb and the nasal mucosa (*35*), and the loss of taste and smell, a characteristic of
150 COVID-19, can thus be explained by nasal infection and subsequent inflammation in the olfactory
151 bulb. Such a scenario is in line with the finding that in all the SARS-CoV-2-exposed macaques
152 immune system activation in the olfactory bulb was evidenced by the presence of T-cells and/or
153 activated microglia.
154 Neuronal transport can also explain why some COVID-19 patients develop Parkinson's disease-
155 like symptoms. Viruses can also, via retrograde transport in parasympathic motor neurons of the
156 nervus vagus to the medulla, pons, and midbrain, reach the substantia nigra in the midbrain (*27,*
157 *36*). Notably, the α-synuclein inclusions were found in the ventral midbrain region of the animals.

158 In humans, these inclusions of accumulated misfolded proteins are associated with Parkinson's
159 disease or Lewy body dementia (*37*).
160 There is a growing concern that symptomatic COVID-19 patients may suffer from long-term
161 consequences (*9, 38*). In this light the finding of Lewy bodies in brains of infected macaques
162 without overt clinical signs is intriguing. Together with signs of inflammation and immune
163 activation in the brains of the macaques this finding may point to a not yet earlier described SARS-
164 CoV-2-induced neurodegenerative process that can explain the neurological symptoms that
165 COVID-19 survivors experience (*39*).
166 Lewy bodies are considered a hallmark for the development of Parkinson's disease, or Lewy body
167 dementia. More confirmation is required, but the observations in the translational macaque
168 models for COVID-19 (*12-14, 40, 41*) can be regarded as a serious warning as they may be
169 predictive for COVID-19-related dementia cases in humans in the future, even after an
170 asymptomatic infection or mild disease process.
171

172 **Materials and Methods**

173 **Animals and SARS-CoV-2 exposure**

174 Four cynomolgus macaques (*Macaca fascicularis*) and four Indian-origin rhesus macaques
175 (*Macaca mulatta*) (Table 1) were selected for this study. All macaques were mature, outbred
176 animals, purpose-bred and socially housed at the BPRC. The animals were in good physical health
177 with normal baseline biochemical and hematological values. All were pair-housed with a socially
178 compatible cage-mate. The animals were offered a daily diet consisting of monkey food pellets
179 (Ssniff, Soest, Germany) supplemented with vegetables and fruit. Enrichment was provided daily

180 in the form of pieces of wood, mirrors, food puzzles, and a variety of other homemade or
181 commercially available enrichment products. Drinking water was available *ad libitum* via an
182 automatic system. Animal Care staff provided daily visual health checks before infection, and
183 twice-daily after infection. The animals were monitored for appetite, general behavior, and stool
184 consistency. All possible precautions were taken to ensure the welfare and to avoid any
185 discomfort to the animals. All experimental interventions (intratracheal and intranasal infection,
186 swabs, blood samplings, and PET-CTs) were performed under anesthesia. The research protocol
187 was approved by national authorities (CCD, Central Committee for Animal Experiments; license
188 number AVD5020020209404). Approval to start was obtained after further assessment of the
189 detailed study protocol by the institutional animal welfare body (AWB) (in Dutch: Instantie voor
190 Dierenwelzijn, IvD). The BPRC is accredited by the American Association for Accreditation of
191 Laboratory Animal Care (AAALAC) International and is compliant with European directive
192 2010/63/EU as well as the "Standard for Humane Care and Use of Laboratory Animals by Foreign
193 Institutions" provided by the Department of Health and Human Services of the US National
194 Institutes of Health (NIH, identification number A5539-01).
195 On day 0, all animals were exposed to a dose of 10^5 $TCID_{50}$ of SARS-CoV-2 (strain
196 BetaCOV/BavPat1/2020), diluted in 5 ml phosphate-buffered saline (PBS). The virus was
197 inoculated via a combination of the intratracheal route (4.5 ml) and intranasal route (0.25 ml per
198 nostril). For the histological examination brains from naive control macaques from the same age
199 were obtained from the BPRC biobank, two cynomolgus, and two rhesus macaques.
200
201 **Positron Emission Tomography – Computed Tomography**

202 Positron Emission Tomography (PET)-computed tomography (CT) data were acquired on multiple
203 time points post-infection using a MultiScan Large Field of View Extreme Resolution Research
204 Imager (LFER) 150 PET-CT (Mediso Medical Imaging Systems Ltd., Budapest, Hungary) as
205 described before (*42*). Animals were fasted overnight (glucose level > 8.5 mmol/l). The animals
206 were sedated with ketamine (10 mg/kg ketamine hydrochloride (Alfasan Nederland BV, Woerden,
207 The Netherlands)) combined with medetomidine hydrochloride (0.05 mg/kg (Sedastart; AST
208 Farma B.V., Oudewater, The Netherlands)) to induce sedation and muscle relaxation, both applied
209 intramuscularly (IM). The animals were positioned head first supine (HFS) with the arms up. The
210 scans were acquired under mechanical ventilation in combination with a forced breathing
211 pattern. For anesthetic maintenance, a minimum alveolar concentration of isoflurane (iso-MAC)
212 of around 0,80%-1.00% was used. The body temperature of the animal was maintained by using
213 the Bair Hugger (3M^{TM}, St Paul, MN, USA) supplied with 43˚C airflow. Typically, around 100 MBq
214 of ^{18}F-FDG was applied intravenously (GE Healthcare, Leiderdorp, NL). Thirty minutes after
215 injection the plateau in tracer activity uptake is reached, subsequently a PET of 15 minutes was
216 acquired. After the scan, upon return to their home cage, atipamezole hydrochloride (Sedastop,
217 ASTFarma B.V., Oudewater, NL, 5 mg/ml, 0.25 mg/kg) was administrated IM to antagonize
218 medetomidine. Afterward the emission data was iteratively reconstructed (OSEM3D, 8 iterations,
219 and 9 subsets) into a single frame PET image normalized and corrected for attenuation, scatter,
220 and random coincidences using a reference CT and corrected for radioactive decay. The analysis
221 was performed in VivoQuant 4.5 (Invicro, Boston, USA). Based on repeatability parameters for
222 correct interpretation of the results, a standardized uptake value (SUV) ratio was used for
223 robustness (*17, 42*). An increased uptake, and pituitary gland hypermetabolism is defined as a

224 SUV_{mean} ratio above 1.5 for the pituitary gland over the surrounding brain in combination with a
225 SUV_{peak} ratio above background levels (>1.0). A group of non-infected control rhesus macaques
226 (n=6) were used to calculate average background uptake of ^{18}F-FDG.
227
228 **Brain tissue collection**
229 Five weeks after virus exposure the macaques were euthanized and the brains were collected for
230 further examination. The right hemisphere was used for RT-qPCR analysis and the left hemisphere
231 was fixed in formalin for histology. Fifteen different regions were collected from the right
232 hemisphere for RT-qPCR analysis: 1) part of the pituitary gland, 2) the olfactory bulb, 3) substantia
233 nigra, 4) medulla oblongata, 5) pons, 6) anterior part of the cerebellum, 7) motor cortex medial,
234 8) sensory cortex, 9) frontal basal cortex, 10) hippocampus, 11) caudate nucleus, 12)
235 hypothalamus, 13) globus pallidus, 14) putamen, and 15) thalamus. For the preparation of
236 paraffin-embedded sections of the formalin-fixed left hemisphere, the cerebrum and cerebellum
237 were dissected in 3-4 mm parts on the anterior-posterior axis. Pituitary gland and olfactory bulb
238 were also embedded. From each part, sections (4 μm) were prepared for different staining
239 methods. Immunohistochemistry stains were used for T-cells (CD3), B-cells (CD20), activated
240 microglia (Mamu-DR), Lewy bodies (α-synuclein ab), and for SARS-CoV-2. Hematoxyline-eosine
241 (HE) staining was used for general morphology.
242
243 **Viral RNA detection in brain tissue**
244 Brain tissue samples were weighed and placed in gentleMACS M tubes (30 mg in 100 μl PBS) and
245 treated using a gentleMACS Tissue Dissociator (protein01 program)(Miltenyi Biotec B.V., Leiden,

246 The Netherlands). Next, the homogenized tissue was centrifuged, and 100 μl supernatant was
247 used for RNA isolation. Viral RNA was isolated from using a QIAamp Viral RNA Mini kit (Qiagen
248 Benelux BV, Venlo, The Netherlands) following the manufacturer's instructions. Viral RNA was
249 reverse-transcribed to cDNA using a Transcriptor First Strand cDNA Synthesis kit (Roche
250 Diagnostics BV, Almere, The Netherlands). Viral RNA was quantified by RT-qPCR specific for RdRp
251 gene of SARS-CoV-2, as described by Corman *et al*. (*43*). The lower detection limit of the RT-qPCR
252 was 3.6 viral RNA copies per reaction. Viral sub-genomic RNA was detected essentially as
253 described by Wölfel *et al.* (*44*). For both assays, RNA standard curves were generated by *in vitro*
254 transcription of the target regions.
255
256 **Tissue preparation for histology**
257 The left hemisphere of the brains, part of the pituitary gland, and one olfactory bulb were fixed
258 in formalin for 24 hours and thereafter stored in buffered PBS. Preserved brains were
259 cryoprotected in 30% w/v sucrose in PBS. The cerebrum was dissected in 12 different parts cut
260 anterior-posterior axis at +10, +8, +5, +1, -3, -6, -8, -11, -14, -18, -22 from Bregma (*45*), the
261 cerebellum and pons were cut in 4 parts. These part were embedded in paraffin. From the eight
262 brain parts in which viral RNA was detected by RT-qPCR, strips of brain sections were sliced into
263 12-series of 4 μm sections for different stains. These parts included the frontal cortex, midbrain
264 parts, cerebellum, pituitary gland, and olfactory bulb. Sections were stained with virus antibody
265 staining for virus detection and immunohistochemistry for immune reaction such as T-cell
266 staining (CD3), B-cell staining (CD20), MHC-II cell staining (HLA-DR). Mirror sections were analyzed
267 with a HE staining for brain morphology.

268

269 **Immunohistochemistry**

270 The optimal concentration was determined for each antibody: CD3 (polyclonal rabbit – anti-
271 human CD3 IgG, cat. no. A045201-2, Agilent Technologies), 1:60; CD20 (monoclonal mouse – anti-
272 human CD20 IgG2a, clone L26, cat. no. M075501-2, Agilent Technologies), 1:800; Mamu-DR
273 (monoclonal mouse – anti-human HLA-DR/DQ- IgG1, clone CR3/43, cat. no. M077501-2, Agilent
274 Technologies), 1:150. For antigen retrieval, a steamer was used. Antigen Retrieval solution: IHC-
275 TEK epitope retrieval solution, ready to use (catno IW-1100, IHC world). All incubation steps were
276 at room temperature unless mentioned otherwise. Additionally, hematoxylin was used as a
277 counterstaining in all protocols. After a dehydration sequence, the slides were mounted in
278 Malinol. The counting of cells was performed in a blind matter.

279

280 *CD3 and CD20 staining*

281 The slides were deparaffinized by putting the slides sequentially in xylene, 100% ethanol, 96%
282 ethanol, 70% ethanol, and PBS. Subsequently, an epitope antigen retrieval was executed in a
283 steamer for 1h. After cooling down, the slides were placed in cuvettes (Sequenza cover plate
284 system productnr 36107 Ted Pella inc.). Endogenous peroxidase (PO) activity was blocked by the
285 PO blocking solution from DAKO (S2023) for 15 minutes. After a washing step (PBS with 0.05%
286 Tween) Avidin was added from the DAKO kit (X0590) for 10 minutes. Thereafter, another washing
287 step and biotin was added from the same DAKO kit (10 min) for blocking endogenous biotine.
288 After washing a blocking step was executed for 20 minutes (PBS with 0.1% BSA and 1% normal
289 human serum, NHS). The primary antibody was added (diluted in 0.1% BSA in PBS) and the slices

290 were left overnight at 4°C. After washing a secondary antibody (Rabbit-anti-mouse IgG
291 biotinylated (E0354), Agilent Technologies; 1:200 diluted in PBS + 1% BSA + 1% NHS) was added
292 and, after washing, the slides were incubated with Vectastain ABC-peroxidase (ABC-PO, from
293 Vector Laboratories; PK-4000; diluted 1:100 in PBS) for 30 minutes. After washing, 3,3'-
294 diaminobenzidine (DAB) with 0.02% H_20_2 was added to visualize the antigen-antibody binding (20
295 min).
296
297 *Mamu-DR staining*
298 The EnVision™ staining kit (G|2 Double-stain System, Rabbit/Mouse, DAB+/Permanent RED code
299 K5361; Agilent technologies, Dako DK) was used for the immunohistochemical stain of Mamu-DR.
300 The slides were deparaffinized by putting them sequentially in xylene, 100% ethanol, 96%
301 ethanol, 70% ethanol, and PBS. Subsequently, an epitope antigen retrieval was executed and the
302 slides were put in a steamer for 1 hour. The cooled down slides were placed in cuvettes and the
303 endogenous peroxidase activity was blocked by the envision kit. The slides were washed and
304 thereafter a blocking step was used consisting of 1% NHS + 1% BSA + 0.2% triton x100 in PBS for
305 10 minutes. Subsequently, the primary antibody was added (diluted in 0.1% BSA/PBS) for 30
306 minutes. Thereafter a washing step was implemented and the EnVision™ polymer/HRP
307 (secondary antibody) was added for 10 minutes. Polymer HRP was added for 10 minutes followed
308 by a washing step. Thereafter DAB+ was added for 15 minutes to visualize the antigen-antibody
309 binding.
310
311 *α-Synuclein staining*

312 The slides were deparaffinized by immersing them sequentially in xylene, 100% ethanol, 96%
313 ethanol, 70% ethanol, and PBS. Subsequently, an epitope antigen retrieval was executed by
314 putting the slides for 15 minutes in Formic acid (100%) diluted 1:10 in demineralized water. After
315 2 washing steps in PBS with 0,05% Tween, the slides were placed in cuvettes (Sequenza cover
316 plate system product no. 36107 Ted Pella inc.). Endogenous PO activity was blocked by the PO
317 blocking solution from DAKO (S2023) for 20 minutes. After washing (PBS with 0.05% Tween),
318 avidin was added from the DAKO kit (X0590) for 10 minutes. Then, after another washing step,
319 biotin was added from the same DAKO kit (10 min) for blocking of endogenous biotine. After
320 washing, a blocking step was executed for 30 minutes (PBS with 0.1% BSA and 1% NHS and 0.02%
321 Triton-X100). The primary antibody, α-synuclein clone 4D6 (Biolegend SIG-39720), was added
322 (diluted in 0.1% BSA in PBS) and the slides were left overnight at 4°C. After washing, a secondary
323 antibody (rabbit anti-mouse IgG Biotinylated (E0354), Agilent Technologies; 1:200 diluted in PBS
324 + 1% BSA) was added for 30 minutes and the slides were incubated with Vectastain ABC-PO kit
325 from Vector Laboraties (PK-4000; diluted 1:100 in PBS) for 30 minutes. After a final washing step,
326 DAB with 0.02% H_20_2 was added to visualize the Antigen-antibody binding (20 min).
327
328 *SARS-CoV-2 staining*
329 The Roche Optiview DAB IHC kit was used in a Ventana Benchmark Ultra (Roche, Basel
330 Switzerland) immunostainer to immunohistochemically stain SARS-CoV-2. Two monoclonal
331 antibodies of ThermoFisher raised to SARS-CoV-2 Nucleocapsid (clone B46F, catno MA1-7404,
332 and E16C, catno. MA1-7403) were validated on formaldehyde-fixed and paraffin-embedded
333 SARS-CoV-2 and mock-infected Vero E6 cells (*10*), as well as lung tissue sections of human SARS-

334 CoV-2 patients. The clone E16C was superior to B46F and was further used in this study. Antigen
335 retrieval took place with cell conditioning 1 (CC1 , Ventana Medical Systems) (pH 8,5) for 24
336 minutes at 100°C, 1/5.000 diluted. Thereafter, incubation took place with the primary antibody
337 for 48 minutes at 36°C followed by standard Optiview detection/visualization with DAB and
338 Copper. After immunohistochemical staining, the sections were dehydrated with grades of
339 ethanol and cleared with xylene. All sections were mounted with TissueTek® coverslipping film
340 (Sakura Finetek Europe B.V., Alphen aan den Rijn, The Netherlands).

341

342 **References**

343 1. V. Coronaviridae Study Group of the International Committee on Taxonomy of, The
344 species Severe acute respiratory syndrome-related coronavirus: classifying 2019-nCoV
345 and naming it SARS-CoV-2. *Nat Microbiol* **5**, 536-544 (2020).
346 2. L. Mao, H. Jin, M. Wang, Y. Hu, S. Chen, Q. He, J. Chang, C. Hong, Y. Zhou, D. Wang, X.
347 Miao, Y. Li, B. Hu, Neurologic Manifestations of Hospitalized Patients With Coronavirus
348 Disease 2019 in Wuhan, China. *JAMA Neurol* **77**, 683-690 (2020).
349 3. R. W. Paterson, R. L. Brown, L. Benjamin, R. Nortley, S. Wiethoff, T. Bharucha, D. L.
350 Jayaseelan, G. Kumar, R. E. Raftopoulos, L. Zambreanu, V. Vivekanandam, A. Khoo, R.
351 Geraldes, K. Chinthapalli, E. Boyd, H. Tuzlali, G. Price, G. Christofi, J. Morrow, P.
352 McNamara, B. McLoughlin, S. T. Lim, P. R. Mehta, V. Levee, S. Keddie, W. Yong, S. A. Trip,
353 A. J. M. Foulkes, G. Hotton, T. D. Miller, A. D. Everitt, C. Carswell, N. W. S. Davies, M.
354 Yoong, D. Attwell, J. Sreedharan, E. Silber, J. M. Schott, A. Chandratheva, R. J. Perry, R.
355 Simister, A. Checkley, N. Longley, S. F. Farmer, F. Carletti, C. Houlihan, M. Thom, M. P.
356 Lunn, J. Spillane, R. Howard, A. Vincent, D. J. Werring, C. Hoskote, H. R. Jager, H. Manji,
357 M. S. Zandi, The emerging spectrum of COVID-19 neurology: clinical, radiological and
358 laboratory findings. *Brain* **143**, 3104-3120 (2020).
359 4. M. Fotuhi, A. Mian, S. Meysami, C. A. Raji, Neurobiology of COVID-19. *J Alzheimers Dis*
360 **76**, 3-19 (2020).
361 5. A. Giacomelli, L. Pezzati, F. Conti, D. Bernacchia, M. Siano, L. Oreni, S. Rusconi, C.
362 Gervasoni, A. L. Ridolfo, G. Rizzardini, S. Antinori, M. Galli, Self-reported Olfactory and
363 Taste Disorders in Patients With Severe Acute Respiratory Coronavirus 2 Infection: A
364 Cross-sectional Study. *Clin Infect Dis* **71**, 889-890 (2020).
365 6. M. E. Cohen, R. Eichel, B. Steiner-Birmanns, A. Janah, M. Ioshpa, R. Bar-Shalom, J. J. Paul,
366 H. Gaber, V. Skrahina, N. M. Bornstein, G. Yahalom, A case of probable Parkinson's
367 disease after SARS-CoV-2 infection. *Lancet Neurol* **19**, 804-805 (2020).

7. I. Faber, P. R. P. Brandao, F. Menegatti, D. D. de Carvalho Bispo, F. B. Maluf, F. Cardoso, Coronavirus Disease 2019 and Parkinsonism: A Non-post-encephalitic Case. *Mov Disord* **35**, 1721-1722 (2020).
8. A. Mendez-Guerrero, M. I. Laespada-Garcia, A. Gomez-Grande, M. Ruiz-Ortiz, V. A. Blanco-Palmero, F. J. Azcarate-Diaz, P. Rabano-Suarez, E. Alvarez-Torres, C. P. de Fuenmayor-Fernandez de la Hoz, D. Vega Perez, R. Rodriguez-Montalban, A. Perez-Rivilla, J. Sayas Catalan, A. Ramos-Gonzalez, J. Gonzalez de la Aleja, Acute hypokinetic-rigid syndrome following SARS-CoV-2 infection. *Neurology* **95**, e2109-e2118 (2020).
9. M. T. Heneka, D. Golenbock, E. Latz, D. Morgan, R. Brown, Immediate and long-term consequences of COVID-19 infections for the development of neurological disease. *Alzheimers Res Ther* **12**, 69 (2020).
10. B. Schurink, E. Roos, T. Radonic, E. Barbe, C. S. C. Bouman, H. H. de Boer, G. J. de Bree, E. B. Bulle, E. M. Aronica, S. Florquin, J. Fronczek, L. M. A. Heunks, M. D. de Jong, L. Guo, R. du Long, R. Lutter, P. C. G. Molenaar, E. A. Neefjes-Borst, H. W. M. Niessen, C. J. M. van Noesel, J. Roelofs, E. J. Snijder, E. C. Soer, J. Verheij, A. P. J. Vlaar, W. Vos, N. N. van der Wel, A. C. van der Wal, P. van der Valk, M. Bugiani, Viral presence and immunopathology in patients with lethal COVID-19: a prospective autopsy cohort study. *Lancet Microbe* **1**, e290-e299 (2020).
11. S. Natoli, V. Oliveira, P. Calabresi, L. F. Maia, A. Pisani, Does SARS-Cov-2 invade the brain? Translational lessons from animal models. *Eur J Neurol* **27**, 1764-1773 (2020).
12. C. Munoz-Fontela, W. E. Dowling, S. G. P. Funnell, P. S. Gsell, A. X. Riveros-Balta, R. A. Albrecht, H. Andersen, R. S. Baric, M. W. Carroll, M. Cavaleri, C. Qin, I. Crozier, K. Dallmeier, L. de Waal, E. de Wit, L. Delang, E. Dohm, W. P. Duprex, D. Falzarano, C. L. Finch, M. B. Frieman, B. S. Graham, L. E. Gralinski, K. Guilfoyle, B. L. Haagmans, G. A. Hamilton, A. L. Hartman, S. Herfst, S. J. F. Kaptein, W. B. Klimstra, I. Knezevic, P. R. Krause, J. H. Kuhn, R. Le Grand, M. G. Lewis, W. C. Liu, P. Maisonnasse, A. K. McElroy, V. Munster, N. Oreshkova, A. L. Rasmussen, J. Rocha-Pereira, B. Rockx, E. Rodriguez, T. F. Rogers, F. J. Salguero, M. Schotsaert, K. J. Stittelaar, H. J. Thibaut, C. T. Tseng, J. Vergara-Alert, M. Beer, T. Brasel, J. F. W. Chan, A. Garcia-Sastre, J. Neyts, S. Perlman, D. S. Reed, J. A. Richt, C. J. Roy, J. Segales, S. S. Vasan, A. M. Henao-Restrepo, D. H. Barouch, Animal models for COVID-19. *Nature* **586**, 509-515 (2020).
13. K. P. Böszörményi, M. A. Stammes, Z. C. Fagrouch, G. Kiemenyi-Kayere, H. Niphuis, D. Mortier, N. van Driel, I. Nieuwenhuis, E. Zuiderwijk-Sick, L. Meijer, P. Mooij, E. J. Remarque, G. Koopman, A. C. R. Hoste, P. Sastre, B. L. Haagmans, R. E. Bontrop, J. A. M. Langermans, W. M. Bogers, E. J. Verschoor, B. E. Verstrepen, Comparison of SARS-CoV-2 infection in two non-human primate species: rhesus and cynomolgus macaques. *bioRxiv*, 11.05.369413 (2020).
14. B. Rockx, T. Kuiken, S. Herfst, T. Bestebroer, M. M. Lamers, B. B. Oude Munnink, D. de Meulder, G. van Amerongen, J. van den Brand, N. M. A. Okba, D. Schipper, P. van Run, L. Leijten, R. Sikkema, E. Verschoor, B. Verstrepen, W. Bogers, J. Langermans, C. Drosten, M. Fentener van Vlissingen, R. Fouchier, R. de Swart, M. Koopmans, B. L. Haagmans, Comparative pathogenesis of COVID-19, MERS, and SARS in a nonhuman primate model. *Science* **368**, 1012-1015 (2020).

411 15. F. Pan, T. Ye, P. Sun, S. Gui, B. Liang, L. Li, D. Zheng, J. Wang, R. L. Hesketh, L. Yang, C.
412 Zheng, Time Course of Lung Changes at Chest CT during Recovery from Coronavirus
413 Disease 2019 (COVID-19). *Radiology* **295**, 715-721 (2020).
414 16. M. Meyer, G. Allenbach, M. Nicod Lalonde, N. Schaefer, J. O. Prior, S. Gnesin, Increased
415 (18)F-FDG signal recovery from small physiological structures in digital PET/CT and
416 application to the pituitary gland. *Sci Rep* **10**, 368 (2020).
417 17. S. Goutal, N. Tournier, M. Guillermier, N. Van Camp, O. Barret, M. Gaudin, M.
418 Bottlaender, P. Hantraye, S. Lavisse, Comparative test-retest variability of outcome
419 parameters derived from brain [18F]FDG PET studies in non-human primates. *PLoS One*
420 **15**, e0240228 (2020).
421 18. R. Pal, M. Banerjee, COVID-19 and the endocrine system: exploring the unexplored. *J*
422 *Endocrinol Invest* **43**, 1027-1031 (2020).
423 19. R. Pal, COVID-19, hypothalamo-pituitary-adrenal axis and clinical implications. *Endocrine*
424 **68**, 251-252 (2020).
425 20. M. W. J. Chua, M. P. W. Chua, Delayed Onset of Central Hypocortisolism in a Patient
426 Recovering From COVID-19. *AACE Clin Case Rep* **7**, 2-5 (2021).
427 21. I. Hamming, W. Timens, M. L. Bulthuis, A. T. Lely, G. Navis, H. van Goor, Tissue
428 distribution of ACE2 protein, the functional receptor for SARS coronavirus. A first step in
429 understanding SARS pathogenesis. *J Pathol* **203**, 631-637 (2004).
430 22. M. Hoffmann, H. Kleine-Weber, S. Schroeder, N. Kruger, T. Herrler, S. Erichsen, T. S.
431 Schiergens, G. Herrler, N. H. Wu, A. Nitsche, M. A. Muller, C. Drosten, S. Pohlmann, SARS-
432 CoV-2 Cell Entry Depends on ACE2 and TMPRSS2 and Is Blocked by a Clinically Proven
433 Protease Inhibitor. *Cell* **181**, 271-280 e278 (2020).
434 23. Z. Walker, K. L. Possin, B. F. Boeve, D. Aarsland, Lewy body dementias. *Lancet* **386**, 1683-
435 1697 (2015).
436 24. M. Sezgin, B. Bilgic, S. Tinaz, M. Emre, Parkinson's Disease Dementia and Lewy Body
437 Disease. *Semin Neurol* **39**, 274-282 (2019).
438 25. T. Yamada, Viral etiology of Parkinson's disease: Focus on influenza A virus. *Parkinsonism*
439 *Relat Disord* **2**, 113-121 (1996).
440 26. R. L. Doty, The olfactory vector hypothesis of neurodegenerative disease: is it viable?
441 *Ann Neurol* **63**, 7-15 (2008).
442 27. I. Mori, Viremic attack explains the dual-hit theory of Parkinson's disease. *Med*
443 *Hypotheses* **101**, 33-36 (2017).
444 28. E. M. Gatto, J. Fernandez Boccazzi, COVID-19 and neurodegeneration: what can we learn
445 from the past? *Eur J Neurol* **27**, e45 (2020).
446 29. A. Y. Vittor, M. Long, P. Chakrabarty, L. Aycock, V. Kollu, S. T. DeKosky, West Nile Virus-
447 Induced Neurologic Sequelae-Relationship to Neurodegenerative Cascades and
448 Dementias. *Curr Trop Med Rep* **7**, 25-36 (2020).
449 30. S. Ait Wahmane, A. Achbani, Z. Ouhaz, M. Elatiqi, A. Belmouden, M. Nejmeddine, The
450 Possible Protective Role of alpha-Synuclein Against Severe Acute Respiratory Syndrome
451 Coronavirus 2 Infections in Patients With Parkinson's Disease. *Mov Disord* **35**, 1293-1294
452 (2020).
453 31. D. K. Singh, B. Singh, S. R. Ganatra, M. Gazi, J. Cole, R. Thippeshappa, K. J. Alfson, E.
454 Clemmons, O. Gonzalez, R. Escobedo, T. H. Lee, A. Chatterjee, Y. Goez-Gazi, R. Sharan,

455 M. Gough, C. Alvarez, A. Blakley, J. Ferdin, C. Bartley, H. Staples, L. Parodi, J. Callery, A.
456 Mannino, B. Klaffke, P. Escareno, R. N. Platt, 2nd, V. Hodara, J. Scordo, S. Gautam, A. G.
457 Vilanova, A. Olmo-Fontanez, A. Schami, A. Oyejide, D. K. Ajithdoss, R. Copin, A. Baum, C.
458 Kyratsous, X. Alvarez, M. Ahmed, B. Rosa, A. Goodroe, J. Dutton, S. Hall-Ursone, P. A.
459 Frost, A. K. Voges, C. N. Ross, K. Sayers, C. Chen, C. Hallam, S. A. Khader, M. Mitreva, T. J.
460 C. Anderson, L. Martinez-Sobrido, J. L. Patterson, J. Turner, J. B. Torrelles, E. J. Dick, Jr., K.
461 Brasky, L. S. Schlesinger, L. D. Giavedoni, R. Carrion, Jr., D. Kaushal, Responses to acute
462 infection with SARS-CoV-2 in the lungs of rhesus macaques, baboons and marmosets.
463 *Nat Microbiol* **6**, 73-86 (2021).
464 32. E. Song, C. Zhang, B. Israelow, A. Lu-Culligan, A. V. Prado, S. Skriabine, P. Lu, O. E.
465 Weizman, F. Liu, Y. Dai, K. Szigeti-Buck, Y. Yasumoto, G. Wang, C. Castaldi, J. Heltke, E.
466 Ng, J. Wheeler, M. M. Alfajaro, E. Levavasseur, B. Fontes, N. G. Ravindra, D. Van Dijk, S.
467 Mane, M. Gunel, A. Ring, S. A. J. Kazmi, K. Zhang, C. B. Wilen, T. L. Horvath, I. Plu, S. Haik,
468 J. L. Thomas, A. Louvi, S. F. Farhadian, A. Huttner, D. Seilhean, N. Renier, K. Bilguvar, A.
469 Iwasaki, Neuroinvasion of SARS-CoV-2 in human and mouse brain. *J Exp Med* **218**,
470 (2021).
471 33. P. A. Swanson, 2nd, D. B. McGavern, Viral diseases of the central nervous system. *Curr*
472 *Opin Virol* **11**, 44-54 (2015).
473 34. E. Lazartigues, M. M. F. Qadir, F. Mauvais-Jarvis, Endocrine Significance of SARS-CoV-2's
474 Reliance on ACE2. *Endocrinology* **161**, bqaa108 (2020).
475 35. J. Meinhardt, J. Radke, C. Dittmayer, J. Franz, C. Thomas, R. Mothes, M. Laue, J.
476 Schneider, S. Brünink, S. Greuel, M. Lehmann, O. Hassan, T. Aschman, E. Schumann, R. L.
477 Chua, C. Conrad, R. Eils, W. Stenzel, M. Windgassen, L. Rößler, H.-H. Goebel, H. R.
478 Gelderblom, H. Martin, A. Nitsche, W. J. Schulz-Schaeffer, S. Hakroush, M. S. Winkler, B.
479 Tampe, F. Scheibe, P. Körtvélyessy, D. Reinhold, B. Siegmund, A. A. Kühl, S. Elezkurtaj, D.
480 Horst, L. Oesterhelweg, M. Tsokos, B. Ingold-Heppner, C. Stadelmann, C. Drosten, V. M.
481 Corman, H. Radbruch, F. L. Heppner, Olfactory transmucosal SARS-CoV-2 invasion as a
482 port of central nervous system entry in individuals with COVID-19. *Nature Neuroscience*
483 **24**, 168-175 (2021).
484 36. C. H. Hawkes, K. Del Tredici, H. Braak, Parkinson's disease: a dual-hit hypothesis.
485 *Neuropathol Appl Neurobiol* **33**, 599-614 (2007).
486 37. J. P. Taylor, J. Hardy, K. H. Fischbeck, Toxic proteins in neurodegenerative disease.
487 *Science* **296**, 1991-1995 (2002).
488 38. M. Marshall, The lasting misery of coronavirus long-haulers. *Nature* **585**, 339-341 (2020).
489 39. J. P. Rogers, A. S. David, A longer look at COVID-19 and neuropsychiatric outcomes.
490 *Lancet Psychiatry* **8**, 351-352 (2021).
491 40. H. Zheng, H. Li, L. Guo, Y. Liang, J. Li, X. Wang, Y. Hu, L. Wang, Y. Liao, F. Yang, Y. Li, S.
492 Fan, D. Li, P. Cui, Q. Wang, H. Shi, Y. Chen, Z. Yang, J. Yang, D. Shen, W. Cun, X. Zhou, X.
493 Dong, Y. Wang, Y. Chen, Q. Dai, W. Jin, Z. He, Q. Li, L. Liu, Virulence and pathogenesis of
494 SARS-CoV-2 infection in rhesus macaques: A nonhuman primate model of COVID-19
495 progression. *PLoS Pathog* **16**, e1008949 (2020).
496 41. V. J. Munster, F. Feldmann, B. N. Williamson, N. van Doremalen, L. Perez-Perez, J. Schulz,
497 K. Meade-White, A. Okumura, J. Callison, B. Brumbaugh, V. A. Avanzato, R. Rosenke, P.

W. Hanley, G. Saturday, D. Scott, E. R. Fischer, E. de Wit, Respiratory disease in rhesus macaques inoculated with SARS-CoV-2. *Nature* **585**, 268-272 (2020).

42. M. A. Stammes, J. Bakker, R. A. W. Vervenne, D. G. M. Zijlmans, L. van Geest, M. P. M. Vierboom, J. A. M. Langermans, F. A. W. Verreck, Recommendations for Standardizing Thorax PET–CT in Non-Human Primates by Recent Experience from Macaque Studies. *Animals* **11**, 204 (2021).

43. V. M. Corman, O. Landt, M. Kaiser, R. Molenkamp, A. Meijer, D. K. Chu, T. Bleicker, S. Brunink, J. Schneider, M. L. Schmidt, D. G. Mulders, B. L. Haagmans, B. van der Veer, S. van den Brink, L. Wijsman, G. Goderski, J. L. Romette, J. Ellis, M. Zambon, M. Peiris, H. Goossens, C. Reusken, M. P. Koopmans, C. Drosten, Detection of 2019 novel coronavirus (2019-nCoV) by real-time RT-PCR. *Euro Surveill* **25**, (2020).

44. R. Wolfel, V. M. Corman, W. Guggemos, M. Seilmaier, S. Zange, M. A. Muller, D. Niemeyer, T. C. Jones, P. Vollmar, C. Rothe, M. Hoelscher, T. Bleicker, S. Brunink, J. Schneider, R. Ehmann, K. Zwirglmaier, C. Drosten, C. Wendtner, Virological assessment of hospitalized patients with COVID-2019. *Nature* **581**, 465-469 (2020).

45. G. Paxinos, X. F. Huang, M. Petrides, A. Toga, *The Rhesus Monkey Brain: in Stereotaxic Coordinates*. (Elsevier Science Publishing Co Inc, San Diego, Ca., ed. 2nd, 2008), pp. 416.

Acknowledgements

We want to thank Francisca van Hassel for assistance with editing of figures, Yolanda Kap for reviewing the manuscript, Wim Vos for the excellent histology, and the Animal Science Department of the BPRC, the veterinarians and animal caretakers for all the experimental support.

Funding

This study was supported by funding from the Biomedical Primate Research Centre. KPB was supported by the European Union's Marie Skłodowska-Curie Innovative Training Network HONOURs; grant agreement no. 721367.

Author contributions

Conceptualization: IHCHMP, EJV, MAS, BEV

Data curation: MAS, BEV, IHCHMP

Formal Analysis: MAS, IHCHMP, BEV

Funding acquisition: EJV

Investigation: KPB, JAW, ZCF, NvD, AQM, DL

533 Methodology: MAS, MB, BS, IHCHMP

534 Project administration: EJV, BEV

535 Resources: REB

536 Supervision: IHCHMP, MAS, BEV, EJV

537 Validation: MB, ER, L-FG-O,

538 Writing – original draft: IHCHMP, KPB

539 Writing – review & editing: MAS, EJV, BEV, JAML, REB, JM, WMB, L-FG-O

540

541 **Competing interests:**

542 The authors declare that they have no competing interests.

543

544 **Data and materials availability:**

545 All data needed to evaluate the conclusions in the paper are present in the paper and/or

546 the Supplementary Materials. Correspondence should be addressed to IHCHMP

547 (philippens@bprc.nl).

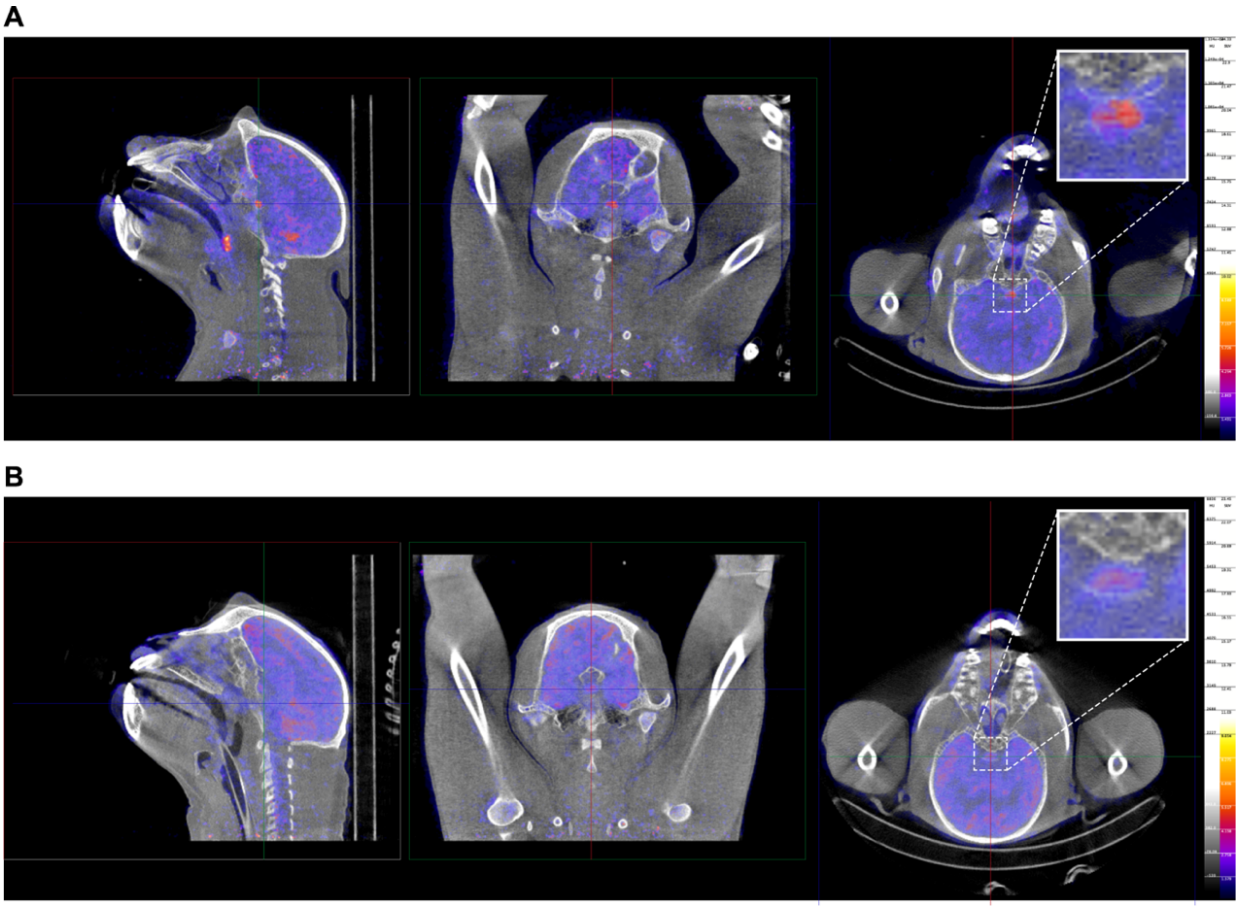

Fig. 1. ^{18}F-FDG PET-CT image of a SARS-CoV-2 infected cynomolgus macaque (C1). Representative images of cynomolgus macaque C1 **(A)** on day 29, and a healthy control animal **(B)** are shown. The pituitary gland is indicated by the cross-hairs in all three directions and is boxed (right pictures). Similar window-level settings are applied for all sections. The pituitary gland-brain ratio of animal C1 was calculated with both the mean and peak standard uptake value (SUV); for the SUV_{mean} this ratio was 1.9, and for the SUV_{peak} 1.3. The average values calculated from a group of non-infected control animals (n=6) were 1.1 (std 0.3) for the SUV_{mean}, and 0.6 (std 0.1) for the SUV_{peak} ratio. The uptake values of the brain, defined as background, were similar with SUV_{mean} values of 2.2 and 1.9 for the SARS-CoV-2-infected animals and the non-infected controls, respectively. After the relevant corrections for attenuation, scatter and decay, our

559 results are indeed indicative for pituitary hypermetabolism after SARS-CoV-2 infection in animals

560 C1 and C2.

561

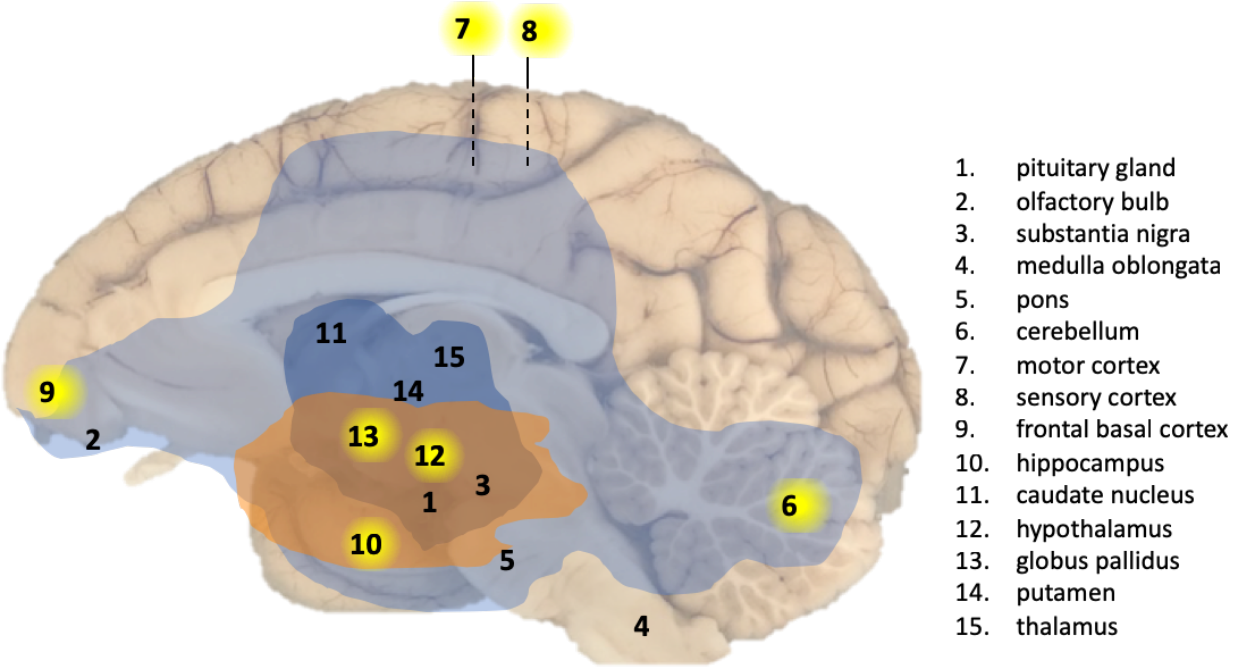

562

563 **Fig. 2. Overview of CNS effects by SARS-CoV-2 exposure in a macaque brain.** Presence of viral

564 RNA was investigated in multiple regions of the brain as indicated by the numbers. Viral RNA-

565 positive regions in cynomolgus macaque C3 are indicated by a yellow background. The analysed

566 brain regions are indicated with a number. Brain areas with T-cells (CD3+) and activated microglia

567 (Mamu-DR+) are shown in light blue (mild expression) and dark blue (moderate expression),

568 respectively. Brain areas with Lewy bodies (α-synuclein+) are shown in orange.

569

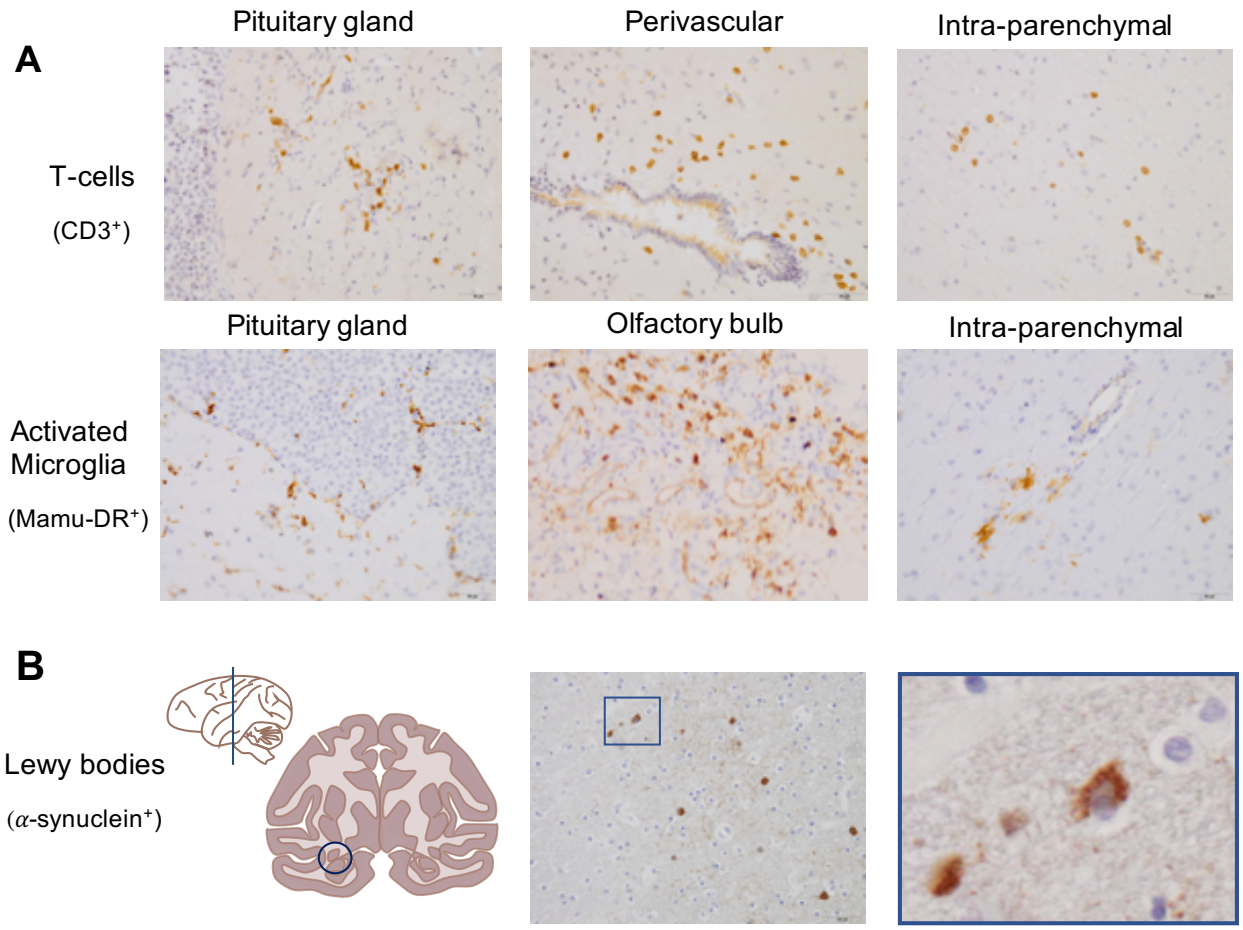

570

571 **Fig. 3. SARS-CoV-2 causes brain inflammation and Lewy body formationin brains of macaques.**

572 Immunohistochemical stainings of macaque brain tissues. **(A)** top panel: T-cells (CD3+) in the

573 pituitary gland (left), perivascular (middle) and in the brain parenchyma (right) from a rhesus

574 macaque (20x). **(A)** middle panel: activated microglia (Mamu-DR+) in the pituitary gland (left),

575 olfactory bulb (middle) and in the brain parenchyma (right) from a cynomolgus macaque (20x).

576 **(B)** bottom panel: Lewy bodies (α-synuclein +) were found in the ventral midbrain region next to

577 the caudate nucleus indicated with a circle (left) in the coronal section of one hemisphere

578 (anterior-posterior 0), presence of Lewy bodies in a SARS-CoV-2-infected rhesus macaque (20x)

579 (middle), a magnified image (40x) of the square in the left image (right).

580

581 **Table 1: Animals featuring in this study**

Macaque species	Monkey ID	Infected Y/N	Age (Year)	Body weight[#] (kg)	Sex M/F
Rhesus	R1	Y	6	8.2	M
Rhesus	R2	Y	5	7.9	M
Rhesus	R3	Y	5	7.8	M
Rhesus	R4	Y	5	8.7	M
Rhesus	control R5	N	5	8.5	M
Rhesus	control R6	N	6	5.1	F
Cynomolgus	C1	Y	4	5.7	M
Cynomolgus	C2	Y	4	3.3	M
Cynomolgus	C3	Y	4	4.9	M
Cynomolgus	C4	Y	16	9.7	M
Cynomolgus	control C5	N	5	5.3	M
Cynomolgus	control C6	N	7	5.1	M

582 [#] at start of study

583 **Table 2**: **Histological findings.**

Marker		Brain area	Rhesus				Cynomolgus				Controls			
			R1	R2	R3	R4	C1	C2	C3	C4	R5	R6	C5	C6
T-cells (CD3+)	intra-parenchymal	pituitary gland												
		olfactory bulb												
		front brain												
		dorsal												
		ventral												
		cerebellum												
	perivascular	pituitary gland												
		olfactory bulb												
		front brain												
		dorsal												
		ventral												
		cerebellum												
	nodules	pituitary gland												
		olfactory bulb												
		front brain												
		dorsal												
		ventral												
		cerebellum												
	meninges	pituitary gland												
		olfactory bulb												
		front brain												
		dorsal												
		ventral												
		cerebellum												
Activated microglia (Mamu-DR+)	presence	pituitary gland												
		olfactory bulb												
		front brain												
		dorsal												
		ventral												
		cerebellum												
	morphology: ramified/ amoeboid	pituitary gland												
		olfactory bulb												
		front brain												
		dorsal												
		ventral												
		cerebellum												
	nodules	pituitary gland												
		olfactory bulb												
		front brain												
		dorsal												
		ventral												
		cerebellum												
	meninges	pituitary gland												
		olfactory bulb												
		front brain												
		dorsal												
		ventral												
		cerebellum												
Lewy bodies (α-synuclein+)	inclusions	ventral midbrain												

584

585 Table 2 outlines the presence of 1) T-cells (CD3+ cells) in the brain tissue (intraparenchymal),

586 around blood vessels (perivascular), in group formation (nodules), or in the meninges, 2) activated

587 microglia (Mamu-DR+ cells) in different parts of the brain, the morphology as a measure for the
588 severity of activation (ramified or amoeboid), in group formation (nodules) or in the meninges, 3)
589 α-synuclein/Lewy bodies (α-synuclein + cells with inclusions) in the ventral midbrain region next
590 to the caudate nucleus. The last column shows the absence of most of these markers in the
591 control animals. Light grey: mild observation; dark grey: moderate observation (including
592 amoeboid microglia cells); black: moderate to severe observation of these markers.
593

Supplementary material:

C1	**SUVmean**					**SUVpeak**				
Tissue/day	*D8/10*	*D16/17*	*D22/23*	*D28/29*	*D35/36*	*D8/10*	*D16/17*	*D22/23*	*D28/29*	*D35/36*
Pituitary gland	3.1	2.5	2.5	3.5	3.9	5.3	3.9	4.1	6.1	6.4
Brain	2.2	1.9	2.4	1.9	2.6	5.0	4.6	4.7	4.6	4.6
Ratio	1.4	1.3	1.0	1.9	1.5	1.1	0.8	0.9	1.3	1.4
C2	**SUVmean**					**SUVpeak**				
Tissue/day	*D8/10*	*D16/17*	*D22/23*	*D28/29*	*D35/36*	*D8/10*	*D16/17*	*D22/23*	*D28/29*	*D35/36*
Pituitary gland	3.1	2.6	2.7	3.8	3.2	7.1	6.3	4.5	6.5	6.1
Brain	2.0	1.8	2.1	2.2	2.1	5.1	3.6	3.8	5.0	3.8
Ratio	1.5	1.5	1.3	1.7	1.5	1.4	1.8	1.2	1.3	1.6

Controls	**SUVmean**						**SUVpeak**					
Tissue/ animal	*NHP1*	*NHP2*	*NHP3*	*NHP4*	*NHP5*	*NHP6*	*NHP1*	*NHP2*	*NHP3*	*NHP4*	*NHP5*	*NHP6*
Pituitary gland	2.3	2.6	2.1	2.7	1.3	1.3	3.3	3.7	2.9	3.9	1.9	1.6
Brain	2.3	2.0	1.9	1.9	1.5	1.8	5.6	6.1	4.9	3.9	3.7	3.5
Ratio	1.0	1.3	1.1	1.4	0.9	0.7	0.6	0.6	0.6	1.0	0.5	0.5

Supplementary Table S1: Quantitative PET-CT analysis of the macaque brains

The standardized uptake values (SUVs) of animals C1 and C2 are represented together with the SUVs of six non-infected control rhesus macaques. Of these animals the average and peak uptake are determined for the pituitary gland, and the brain minus the pituitary gland. By dividing these the pituitary gland/brain ratio is calculated. For the SUVmean values above 1.0 are defined as slightly increased (light grey) and increased (dark grey) when equal or above 1.5. For the SUVpeak values above 1.0 are demarcated as slightly increased and above 1.2 as increased.